New constraints on ultraheavy dark matter from the LZ experiment

J. Aalbers,[1,2] D. S. Akerib,[1,2] A. K. Al Musalhi,[3] F. Alder,[3] C. S. Amarasinghe,[4,5] A. Ames,[1,2] T. J. Anderson,[1,2] N. Angelides,[6] H. M. Araújo,[6] J. E. Armstrong,[7] M. Arthurs,[1,2] A. Baker,[6] S. Balashov,[8] J. Bang,[9] E. E. Barillier,[5,10] J. W. Bargemann,[4] A. Baxter,[11] K. Beattie,[12] T. Benson,[13] A. Bhatti,[7] A. Biekert,[12,14] T. P. Biesiadzinski,[1,2] H. J. Birch,[5,10] E. J. Bishop,[15] G. M. Blockinger,[16] B. Boxer,[17] C. A. J. Brew,[8] P. Brás,[18] S. Burdin,[11] M. Buuck,[1,2] M. C. Carmona-Benitez,[19] M. Carter,[11] A. Chawla,[20] H. Chen,[12] J. J. Cherwinka,[13] Y. T. Chin,[19] N. I. Chott,[21] M. V. Converse,[22] A. Cottle,[3] G. Cox,[23] D. Curran,[23] C. E. Dahl,[24,25] A. David,[3] J. Delgaudio,[23] S. Dey,[26] L. de Viveiros,[19] L. Di Felice,[6] C. Ding,[9] J. E. Y. Dobson,[27] E. Druszkiewicz,[22] S. R. Eriksen,[28] A. Fan,[1,2] N. M. Fearon,[26] S. Fiorucci,[12] H. Flaecher,[28] E. D. Fraser,[11] T. M. A. Fruth,[29] R. J. Gaitskell,[9] A. Geffre,[23] J. Genovesi,[21] C. Ghag,[3] R. Gibbons,[12,14] S. Gokhale,[30] J. Green,[26] M. G. D. van der Grinten,[8] J. H. Haiston,[21] C. R. Hall,[7] S. Han,[1,2] E. Hartigan-O'Connor,[9] S. J. Haselschwardt,[12] M. A. Hernandez,[5,10] S. A. Hertel,[31] G. Heuermann,[5] G. J. Homenides,[32] M. Horn,[23] D. Q. Huang,[5] D. Hunt,[26] C. M. Ignarra,[1,2] E. Jacquet,[6] R. S. James,[3] J. Johnson,[17] A. C. Kaboth,[20] A. C. Kamaha,[33] M. Kannichankandy,[16] D. Khaitan,[22] A. Khazov,[8] I. Khurana,[3] J. Kim,[4] J. Kingston,[17] R. Kirk,[9] D. Kodroff,[19,12] L. Korley,[5] E. V. Korolkova,[34] H. Kraus,[26] S. Kravitz,[12,35] L. Kreczko,[28] B. Krikler,[28] V. A. Kudryavtsev,[34] J. Lee,[36] D. S. Leonard,[36] K. T. Lesko,[12] C. Levy,[16] J. Lin,[12,14] A. Lindote,[18] R. Linehan,[1,2] W. H. Lippincott,[4] M. I. Lopes,[18] E. Lopez Asamar,[18] W. Lorenzon,[5] C. Lu,[9] S. Luitz,[1] P. A. Majewski,[8] A. Manalaysay,[12] R. L. Mannino,[38] C. Maupin,[23] M. E. McCarthy,[22] G. McDowell,[5] D. N. McKinsey,[12,14] J. McLaughlin,[24] J. B. McLaughlin,[3] R. McMonigle,[16] E. H. Miller,[1,2] E. Mizrachi,[7,38] A. Monte,[4] M. E. Monzani,[1,2,39] J. D. Morales Mendoza,[1,2] E. Morrison,[21] B. J. Mount,[40] M. Murdy,[31] A. St. J. Murphy,[15] A. Naylor,[34] C. Nedlik,[31] H. N. Nelson,[4] F. Neves,[18] A. Nguyen,[15] J. A. Nikoleyczik,[13] I. Olcina,[12,14,*] K. C. Oliver-Mallory,[6] J. Orpwood,[34] K. J. Palladino,[26] J. Palmer,[20] N. J. Pannifer,[28] N. Parveen,[16] S. J. Patton,[12] B. Penning,[5,10] G. Pereira,[18] E. Perry,[3] T. Pershing,[38] A. Piepke,[32] Y. Qie,[22] J. Reichenbacher,[21] C. A. Rhyne,[9] Q. Riffard,[12] G. R. C. Rischbieter,[5,10] H. S. Riyat,[15] R. Rosero,[30] T. Rushton,[34] D. Rynders,[23] D. Santone,[20] A. B. M. R. Sazzad,[32] R. W. Schnee,[21] S. Shaw,[15] T. Shutt,[1,2] J. J. Silk,[7] C. Silva,[18] G. Siney,[21] J. Siniscalco,[3] R. Smith,[12,14,†] V. N. Solovov,[18] P. Sorensen,[12] J. Soria,[12,14] I. Stancu,[32] A. Stevens,[3,6] K. Stifter,[25] B. Suerfu,[12,14] T. J. Sumner,[6] M. Szydagis,[16] W. C. Taylor,[9] D. R. Tiedt,[23] M. Timalsina,[12,21] Z. Tong,[6] D. R. Tovey,[34] J. Tranter,[34] M. Trask,[4] M. Tripathi,[17] D. R. Tronstad,[21] W. Turner,[11] A. Vacheret,[6] A. C. Vaitkus,[9] O. Valentino,[6] V. Velan,[12] A. Wang,[1,2] J. J. Wang,[32] Y. Wang,[12,14] J. R. Watson,[12,14] R. C. Webb,[41] L. Weeldreyer,[32] T. J. Whitis,[4] M. Williams,[5] W. J. Wisniewski,[1] F. L. H. Wolfs,[22] S. Woodford,[11] D. Woodward,[19,12] C. J. Wright,[28] Q. Xia,[12] X. Xiang,[9,30] J. Xu,[37] M. Yeh,[30] and E. A. Zweig[33]

(LZ Collaboration)

[1]*SLAC National Accelerator Laboratory, Menlo Park, California 94025-7015, USA*
[2]*Kavli Institute for Particle Astrophysics and Cosmology, Stanford University, Stanford, California 94305-4085 USA*
[3]*Department of Physics and Astronomy, University College London (UCL), London WC1E 6BT, United Kingdom*
[4]*Department of Physics, University of California, Santa Barbara, Santa Barbara, California 93106-9530, USA*
[5]*Randall Laboratory of Physics, University of Michigan, Ann Arbor, Michigan 48109-1040, USA*
[6]*Physics Department, Blackett Laboratory, Imperial College London, London SW7 2AZ, United Kingdom*
[7]*Department of Physics, University of Maryland, College Park, Maryland 20742-4111, USA*
[8]*STFC Rutherford Appleton Laboratory (RAL), Didcot, OX11 0QX, United Kingdom*
[9]*Department of Physics, Brown University, Providence, Rhode Island 02912-9037, USA*
[10]*Department of Physics, University of Zurich, 8057 Zurich, Switzerland*
[11]*Department of Physics, University of Liverpool, Liverpool L69 7ZE, United Kingdom*
[12]*Lawrence Berkeley National Laboratory (LBNL), Berkeley, California 94720-8099, USA*
[13]*Department of Physics, University of Wisconsin-Madison, Madison, Wisconsin 53706-1390, USA*
[14]*Department of Physics, University of California, Berkeley, Berkeley, California 94720-7300, USA*
[15]*SUPA, School of Physics and Astronomy, University of Edinburgh, Edinburgh EH9 3FD, United Kingdom*
[16]*Department of Physics, University at Albany (SUNY), Albany, New York 12222-0100, USA*
[17]*Department of Physics, University of California, Davis, Davis, California 95616-5270, USA*
[18]*Laboratório de Instrumentação e Física Experimental de Partículas (LIP), University of Coimbra, P-3004 516 Coimbra, Portugal*

[19]*Department of Physics, Pennsylvania State University, University Park, Pennsylvania 16802-6300, USA*
[20]*Department of Physics, Royal Holloway, University of London, Egham, TW20 0EX, United Kingdom*
[21]*South Dakota School of Mines and Technology, Rapid City, South Dakota 57701-3901, USA*
[22]*Department of Physics and Astronomy, University of Rochester, Rochester, New York 14627-0171, USA*
[23]*South Dakota Science and Technology Authority (SDSTA), Sanford Underground Research Facility, Lead, South Dakota 57754-1700, USA*
[24]*Department of Physics and Astronomy, Northwestern University, Evanston, Illinois 60208-3112, USA*
[25]*Fermi National Accelerator Laboratory (FNAL), Batavia, Illinois 60510-5011, USA*
[26]*Department of Physics, University of Oxford, Oxford OX1 3RH, United Kingdom*
[27]*Department of Physics, King's College London, London WC2R 2LS, United Kingdom*
[28]*H. H. Wills Physics Laboratory, University of Bristol, Bristol, BS8 1TL, United Kingdom*
[29]*School of Physics, The University of Sydney, Physics Road, Camperdown, Sydney, New South Wales 2006, Australia*
[30]*Brookhaven National Laboratory (BNL), Upton, New York 11973-5000, USA*
[31]*Department of Physics, University of Massachusetts, Amherst, Massachusetts 01003-9337, USA*
[32]*Department of Physics and Astronomy, University of Alabama, Tuscaloosa, Alabama 34587-0324, USA*
[33]*Department of Physics and Astronomy, University of Califonia, Los Angeles, Los Angeles, California 90095-1547*
[34]*Department of Physics and Astronomy, University of Sheffield, Sheffield S3 7RH, United Kingdom*
[35]*Department of Physics, University of Texas at Austin, Austin, Texas 78712-1192, USA*
[36]*IBS Center for Underground Physics (CUP), Yuseong-gu, Daejeon, Korea*
[37]*Laboratório de Instrumentação e Física Experimental de Partículas (LIP), University of Coimbra, P-3004 516 Coimbra, Portugal*
[38]*Lawrence Livermore National Laboratory (LLNL), Livermore, California 94550-9698, USA*
[39]*Vatican Observatory, Castel Gandolfo, V-00120, Vatican City State*
[40]*School of Natural Sciences, Black Hills State University, Spearfish, South Dakota 57799-0002, USA*
[41]*Department of Physics and Astronomy, Texas A & M University, College Station, Texas 77843-4242, USA*

(Received 26 February 2024; accepted 29 April 2024; published 11 June 2024)

Searches for dark matter with liquid xenon time projection chamber experiments have traditionally focused on the region of the parameter space that is characteristic of weakly interacting massive particles, ranging from a few GeV$/c^2$ to a few TeV$/c^2$. Models of dark matter with a mass much heavier than this are well motivated by early production mechanisms different from the standard thermal freeze-out, but they have generally been less explored experimentally. In this work, we present a reanalysis of the first science run of the LZ experiment, with an exposure of 0.9 tonne × yr, to search for ultraheavy particle dark matter. The signal topology consists of multiple energy deposits in the active region of the detector forming a straight line, from which the velocity of the incoming particle can be reconstructed on an event-by-event basis. Zero events with this topology were observed after applying the data selection calibrated on a simulated sample of signal-like events. New experimental constraints are derived, which rule out previously unexplored regions of the dark matter parameter space of spin-independent interactions beyond a mass of 10^{17} GeV$/c^2$.

DOI: 10.1103/PhysRevD.109.112010

I. INTRODUCTION

The astrophysical evidence for the existence of dark matter (DM) is widespread [1–3]. Despite the abundance of indirect evidence manifested through the gravitational effects of dark matter on luminous matter, its nature remains elusive [4,5]. New particles have been invoked to explain this puzzle, with the weakly interacting massive particle (WIMP) and the QCD axion being two of the most popular candidates [6,7]. However, searches for these two particles have so far come back empty-handed [8,9].

The LZ experiment recently set the most stringent limit on the spin-independent DM-nucleon cross section in its first WIMP search run [10]. The LZ experiment is located on the Davis Campus at the Sanford Underground Research Facility in Lead, South Dakota (U.S.). It employs a large,

*ibles10@berkeley.edu
†ryansmith63@berkeley.edu

dual-phase time projection chamber (TPC) of approximately 1.5 m in diameter and height, containing seven active tonnes of liquid xenon (LXe). It features two additional detectors: an instrumented "skin" of LXe used to veto γ-ray and neutron interactions around the active region, and an outer detector (OD) surrounding the TPC that is highly efficient at tagging neutrons and γ rays escaping the TPC. A full description of the LZ experiment can be found in Ref. [11].

In the present work, we consider the search for ultraheavy dark matter particles with the LZ experiment using the same dataset that was used to search for WIMPs in science run 1 (SR1) [10] with an overall exposure of 0.9 tonne × yr. Several mechanisms to create such heavy particles in the early Universe have been proposed [12,13]. For example, the unitary limit imposed on particles produced by thermal freeze-out can be circumvented with composite dark matter models in which light constituents fused together relatively late in the history of the Universe [14–20]. Astrophysical constraints on high-mass dark matter interactions with nuclei exist, but they are rather weak, arising mainly from observations of gas clouds [21], cosmic rays [22,23], white dwarf explosions [24], and ancient mica [25].

As opposed to WIMPs, particles in the high-mass region of the parameter space lose only a small fraction of their energy with each scattering interaction with Standard Model particles. In addition, they are likely to scatter several times inside a detector, creating a tracklike event. These particles are commonly known as multiply interacting massive particles (MIMPs) [26]. At the astrophysical level, MIMPs are expected to act as collisionless, pointlike particles, likewise WIMPs [27]. A few experimental searches for MIMPs already exist [28–33], but they are noticeably small in number compared to WIMP searches.

The paper is organized as follows: in Sec. II we describe the main features of a MIMP interaction in the LZ experiment. We present the data selection in Sec. III, discuss the main findings in Sec. IV, and conclude in Sec. V.

II. SIGNAL TOPOLOGY

A single scatter (SS) in the active region of the TPC results in a prompt scintillation signal in the liquid phase (S1) and a secondary proportional scintillation signal in the gaseous phase (S2). The second light signal is created via electroluminescence from ionization electrons that are drifted through the liquid by an applied electric field and subsequently extracted to the gaseous phase. These light signals are observed by two arrays of photomultiplier tubes (PMTs) located at the top and bottom of the TPC. The integrated waveform area is reported in photons detected (phd) at each PMT. The location of an energy deposit in the TPC is reconstructed from the time difference between the S1 and S2 signals (z coordinate) and the spatial distribution of the S2 signal in the top PMT array (x and y coordinates).

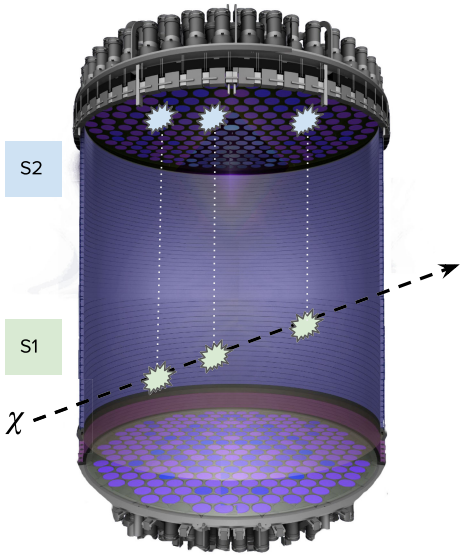

FIG. 1. Illustration of a MIMP crossing the TPC of the LZ experiment and creating three distinct scatters in the active region. Each of these energy depositions is observed as a pair of S1 and S2 light signals in the liquid and gas regions, respectively.

In the region of the DM parameter space explored in the search for WIMPs by LZ in Ref. [10], with masses around 100 GeV/c^2 and WIMP-nucleon interaction cross sections of the order of 10^{-47} cm^2, the flux of transits of dark matter across the detector is relatively high, but the probability that any given transit results in a single scatter is very low. By contrast, in the region of high mass ($> 10^4$ GeV/c^2) and high cross section ($> 10^{-31}$ cm^2) of the dark matter parameter space, the expected flux of dark matter transits is heavily reduced due to the low DM number density, but each of them is expected undergo multiple scatters (MSs) inside the detector [26]. Consequently, a dedicated analysis looking for multiple-scatter events is required to search for MIMPs. It is important to note that scatters from a transiting MIMP would form a straight line given that the angular deflection in each interaction is vanishingly small for dark matter masses much heavier than the xenon nucleus [34].

A diagram of this signal topology is shown in Fig. 1. Multiple S1 pulses occur in a short period of time (typically a few microseconds) and are followed by multiple S2 pulses occurring over the following few hundreds of microseconds. The time separation between the S1 pulses is determined by the arrival times of each scatter, while the time between S2 pulses is determined by the scatter depths [35,36]. Importantly, the positions measured from the S2 pulses and the times measured by the S1 pulses can be used to reconstruct both the magnitude and direction of the velocity vector on an event-by-event basis.

The experimental signature of multiple S1s and multiple S2s forming a track is rather extraordinary. There are only a limited number of processes that could mimic this signature. First, muons can create events with multiple S2s.

However, muons deposit large amounts of energy in the detector, of order of hundreds of MeV, and they can be easily tagged by the external veto detectors. Second, the correlated radiogenic emission of the ^{214}Bi–^{214}Po and ^{212}Bi–^{212}Po decays, originating in the ^{238}U and ^{232}Th decay chains. These β-to-α reactions have a characteristic time correlation of 164 μs and 300 ns, respectively [37,38]. The correlation times are short enough to make it likely that the second decay occurs within the same event window (of 4.5 ms duration), but long enough to allow for the S1 pulses to be resolvable. Events like these are easy to tag and can be excluded with more than 99.99% efficiency [39]. In addition, the energy deposited by the emitted particles is an order of magnitude larger than that of a recoil energy produced by a MIMP and they are expected to occur in the same physical location. Therefore, they do not constitute a relevant source of background for this search. Third, γ rays and neutrons may scatter at multiple resolvable positions in the detector, producing multiple S2s. However, γ-ray or MeV neutrons move too quickly (covering the full 1.5 m dimensions of LZ in under 5 ns) for the multiple scatters they may deposit to produce separate S1s. Slower neutrons moving at velocities consistent with a MIMP signal have insufficient kinetic energy to produce above-threshold nuclear recoil signals. Moreover, neutrons scatter by forming an erratic pattern rather than a straight line due to the low mass of a neutron with respect to the xenon nucleus, which makes them easy to reject. Overall, the expected sources of background for the MIMP search are limited to rare cases of pulse pileup from accidental coincidences [40]. We estimate that the pileup of single-scatter events in the SR1 exposure yields less than 0.17 events, rendering the total background rate negligible.

Prior to searching for MIMPs in the LZ SR1 data, we studied the signal topology in detail with a simulated sample of tracklike events traversing the detector. We used an LZ-specific software package to simulate DM transits across the TPC. Velocities and incident angles were sampled randomly from the standard halo model (SHM) velocity distribution [41] and propagated through to the detector assuming the same parametric model of the LZ detector used for the WIMP search [10]. Since the DM energy spectrum is independent of mass in the high-mass limit, we assumed a fixed dark matter mass of 10^{17} GeV/c^2 and varied the DM-nucleon cross section.

Pulses that arrive closely spaced in time relative to the pulse width may not be resolved by the LZ pulse finder algorithm, and therefore, it is especially important to the MIMP search that the simulations account for this pulse merging effect. LZ's parametric simulation model determines pulses to be merged based on their separation in time, width, and relative pulse area [42,43]. Generally, pulses merge when their separation in arrival time is below approximately 200 ns for S1s and 2 μs for S2s. The effects of pulse merging are illustrated in Fig. 2, which shows the

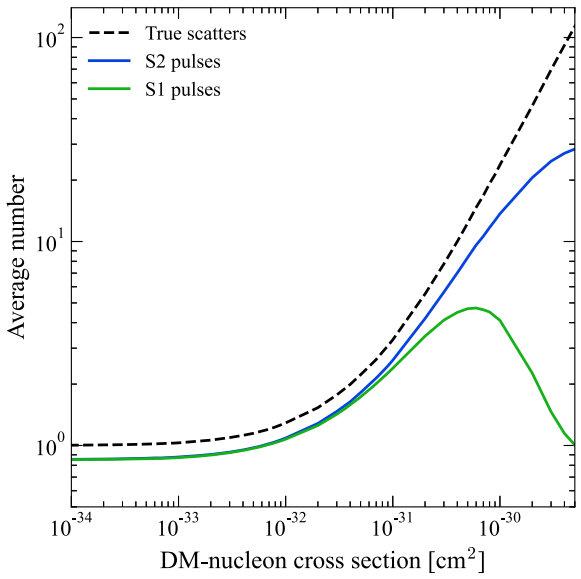

FIG. 2. Average number of reconstructed S1 (green), S2 (blue), and true scatters (black) in simulated events as a function of the spin-independent DM-nucleon cross section assuming a DM mass of 10^{17} GeV/c^2. The simulated events are required to have at least one true scatter. However, note that not all simulated scatters will produce both an S1 and an S2 pulse. The LZ pulse reconstruction software starts merging S1 pulses at lower cross sections than S2 pulses.

average number of true scatters, reconstructed S1 pulses, and reconstructed S2 pulses as a function of the spin-independent DM-nucleon cross section. Above a cross section of 10^{-30} cm^2, the average number of reconstructed S1 pulses in a simulated MIMP event starts to decrease due to pulse merging. Generally, S2 pulses are more easily resolved than S1 pulses due to their larger separation in time. The maximum cross section probed in this analysis is 10^{-29} cm^2, above which the S1 and S2 pulses in a MIMP event are exceedingly unlikely to be reconstructed as individual pulses.

Given the relatively high cross sections probed in this search, it is also important to consider the significance of Earth's shielding, referred to as the overburden. To determine the overburden boundary, we performed simulations of the MIMP flux from every direction for different mass and cross section values in the dark matter parameter space. We set the overburden boundary along those points in the parameter space where less than 1 in 10^5 dark matter particles propagated through Earth maintain a sufficiently large velocity to cause a deposit in the LZ experiment with an energy above 1 keV. For cross sections below our maximum search value of 10^{-29} cm^2, we find that the overburden boundary is only relevant for masses below approximately 10^5 GeV/c^2. Note that at that mass regime the expected number of dark matter transits in LZ without considering the overburden is much greater than 10^5. However, we decided to choose the conservative value

of 10^5 trials to optimize the use of limited computational resources. For more details on the simulation procedure, please see Ref. [44].

III. METHODOLOGY

The SR1 dataset was acquired during a period of 116 calendar days. Of that period, approximately 89 live days were dedicated to acquiring WIMP search data. That period is reduced down to 60 live days after applying data quality cuts designed to exclude periods in which the detector environment was unsuitable for conducting a physics search [10]. Most notably, hold-off times of tens of milliseconds were excluded after large S2s, which are known to be typically followed by elevated photon and electron emission rates [45]. Moreover, periods of time immediately after a muon was tagged by LZ's veto system were removed. The strategy employed in Ref. [10] to search for WIMPs was to look for single-scatter events uniformly distributed in the TPC with no accompanying signals in either of the veto detectors (skin or OD). A strict data selection in the region-of-interest (ROI) of 3–80 phd in corrected S1 area, > 600 phd in uncorrected S2 area (equivalent to 10 extracted electrons), and $< 10^5$ phd in corrected S2 area was applied. Moreover, a profile likelihood ratio (PLR) analysis was conducted to evaluate the compatibility of the surviving single-scatter events with LZ's WIMP search background model, described in Ref. [40]. By contrast, in the MIMP search we look for multiple-scatter events of the kind described in Sec. II and design data quality cuts that are as loose as possible to minimize the reduction of the signal detection efficiency. We start with the same 60 live day dataset, referred to as the "initial selection," and introduce new data selection criteria specific to the MIMP search. To mitigate experimenter bias, we calibrated the data selection on a simulated dataset before applying it to the observed dataset. Furthermore, and given the remarkable topology of the sought-after signal, we set deliberately loose cut boundaries.

The first MIMP-specific cut we apply to the data is the "multiplicity" cut, which ensures that more than 1 S1 and more than 1 S2 pulses are registered in the event. Then, the "good S1" cut is applied to select S1 pulses of a certain quality according to two criteria: first, we only accept S1 pulses in which the observed light is not overly concentrated in one PMT; second, we veto events that have a nearly coincident signal with the outer detector within a few hundred nanoseconds around the S1 arrival time (following the same strategy that was devised for the SR1 WIMP search [10]). It is important to note that we do not consider possible MIMP interactions in either the skin or the OD.

A "fiducial" cut is applied to take advantage of the reduced radioactivity of the inner volume of the detector due to self-shielding. Events are required to have at least two S2 pulses reconstructed within the fiducial volume. This volume is defined by a cylinder approximating the WIMP search fiducial volume [10], albeit slightly expanded —the extraordinary signature of a MIMP signal compared to a WIMP affords some extra lenience in the fiducialization. Elevated rates outside the fiducial volume make pileup of those events more likely. Additionally, the cut at the top of the detector mitigates a prominent background source of event misreconstruction due to interactions that occur in the gas phase. The fiducial region is defined by a radius of 70 cm from the center and a bottom and a top that are 2 and 135 cm above the cathode, respectively.

MIMPs are not expected to be noticeably deflected by xenon atoms as they transit LZ. We exploit this feature by introducing a "collinearity" cut. The collinearity of the scatter positions reconstructed from each S2 in a candidate MIMP track is evaluated in two steps. First, a weighted orthogonal distance regression of the xy coordinates of each S2 is performed. We adopt the same S2 position resolution model described in Ref. [40]. The xy collinearity cut is placed on the corresponding reduced χ^2 value. We apply an upper boundary of reduced χ^2 equal to 2, informed by the reduced χ^2 distribution of simulated MIMP-like events at a DM-nucleon cross section of 10^{-30} cm^2 (which is near the peak S2 pulse multiplicity, see Fig. 2). Second, we check that the ordering of S2 pulses along the length of the track is monotonic. Events with exactly two S2s pass the collinearity cut trivially.

If an event passes the collinearity cut, a three-dimensional best fit track is calculated, along with regressed positions $\mathbf{s}_i$ of each scatter along this track.

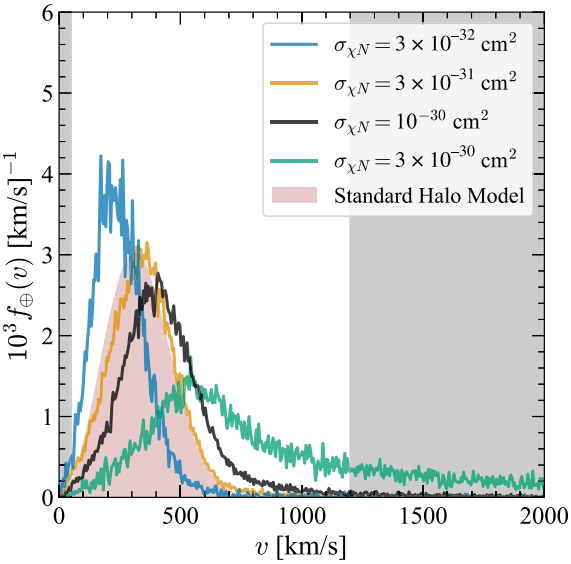

FIG. 3. Reconstructed velocities for simulated MIMP events with DM-nucleon cross sections 3×10^{-32} (blue), 3×10^{-31} (gold), 10^{-30} (black), 3×10^{-30} cm^2 (green) for a DM mass of 10^{17} GeV/c^2. The standard halo model velocity distribution is shown as the shaded red region for reference. The exclusion regions imposed by the velocity cut are indicated by the shaded gray areas.

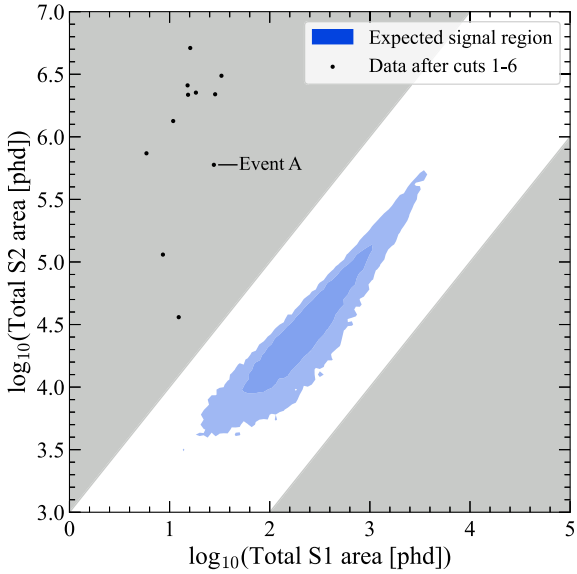

FIG. 4. Cut boundaries for the ROI cut in the space of total S1 area and total S2 area. The excluded regions are indicated by the gray areas. The 68% and 95% contours of the population of simulated MIMPs with a cross section of 10^{-30} cm^2 are shown in light and dark blue, respectively. Events passing all the data analysis cuts before this one are shown as black points. The S1 and S2 pulses of one of the points (event A) are displayed in Fig. 5.

Here i ranges from 1 to the total number N of S2 pulses in the event, with the ordering determined by the distance along the track. A test of the "uniformity" of the scatters along the track is performed in this one-dimensional position space. An estimate of the mean free path (λ) is provided by the distance between the furthest apart scatters divided by the number of gaps between scatters,

$$\lambda = \frac{|\mathbf{s}_N - \mathbf{s}_1|}{N-1}. \tag{1}$$

Then, the distance between scatters, along with the distance between the end point scatters and the extrapolated intersections with the TPC boundary, are compared to λ. The event is rejected if the largest gap exceeds a distance of 20λ or the smallest gap is lower than 0.01λ.

Additionally, we use a "velocity" cut to compare the reconstructed velocity of the candidate MIMP event to the expected dark matter velocity distribution in the Galactic halo. The regressed positions $\mathbf{s}_i$ are used to estimate the magnitude of the velocity vector of the MIMP particle,

$$v = \frac{|\mathbf{s}_N - \mathbf{s}_1|}{t_N - t_1}, \tag{2}$$

where the times t_1 and t_N are the arrival times of the first and last S1 pulses, respectively. This reconstructed velocity metric is subject to some deviation from the true one. For instance, two nearby scatters can cause merged pulses, and some scatters may not produce both an S1 and S2 pulse above threshold. Both effects are more likely to result in the loss of S1s than S2s, which causes the velocity to be overestimated due to the reduction in time between the reconstructed S1 pulses. The velocity cut is based on the distribution of simulated reconstructed velocities, which is generally broader than the true incident velocity distribution. Figure 3 shows the reconstructed velocity distribution of MIMP-like events for four different spin-independent DM-nucleon cross sections. Reconstructed velocities below 50 and above 1200 km/s are considered invalid MIMP candidates. These values are based on the tails of the reconstructed velocity distribution (0.4 and 96.6 percentiles), for the reference cross section of 10^{-30} cm^2 (above this cross section, S1 pulses are likely to start merging, as shown in Fig. 2). Note that the blue histogram representing the lower cross section of 3×10^{-32} cm^2 peaks at a lower velocity than the SHM (shown in red) because of the v^{-2}

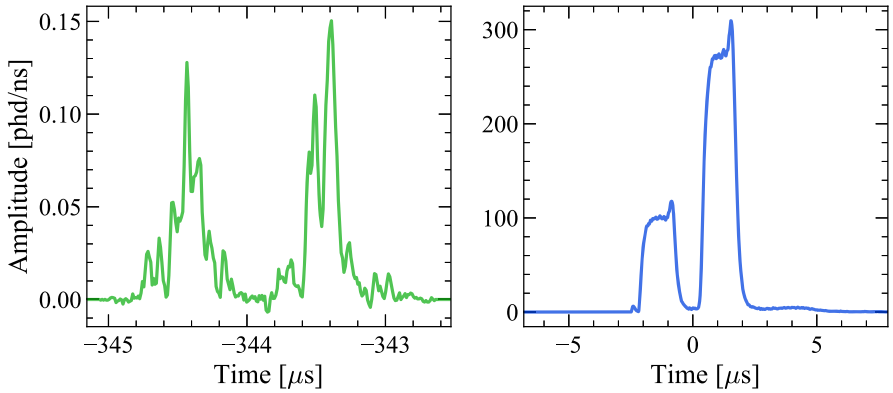

FIG. 5. S1 and S2 waveforms for event A highlighted in Fig. 4. A total of two S1 and two S2 pulses were reconstructed in this event, respectively. The narrow, flat-top shape of the S2 pulses is characteristic of an energy deposit occurring near the liquid surface. The two S1 pulses shown on the left cannot originate from the same energy deposit that created the S2 pulses given their time separation. This event is removed by the ROI cut.

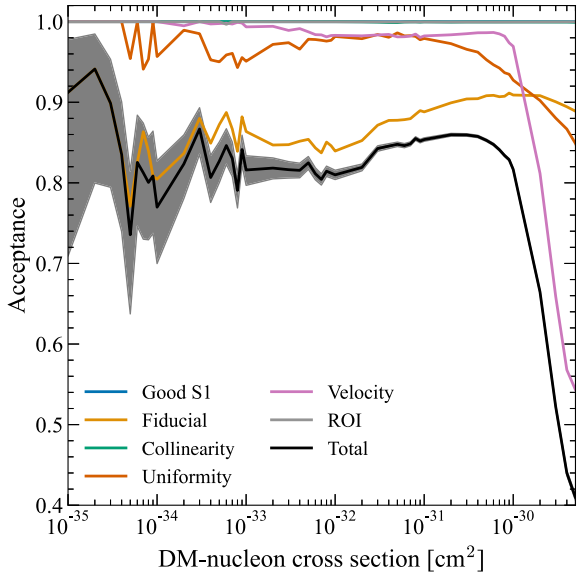

FIG. 6. Acceptance of the cuts listed in Table I as a function of the DM-nucleon scattering cross section evaluated on a simulated dataset of MIMP-like events of mass 10^{17} GeV/c^2. Each colored line shows the acceptance conditional on applying the previous listed cuts. By contrast, the black line shows the total acceptance with respect to the initial selection. A 1σ binomial uncertainty band is indicated in gray. The acceptance is generally high except for cross sections larger than 10^{-30} cm^2, when most events start failing the velocity cut (pink).

dependence of the differential DM-nucleus cross section [46–48], favoring the detection of slower MIMPs.

Finally, we apply an ROI cut that restricts the search space of total S1 and S2 areas. This cut is set conservatively based on the expected distribution of simulated MIMP events in the space of total S1 area and total S2 area, shown in Fig. 4. The events surviving the previously described data analysis cuts are shown as black points. All events are distributed in the excluded region of small summed S1 sizes and large ($> 10^5$ phd) summed S2 sizes. This is characteristic of pileup backgrounds, rather than MIMP-like events. As an example, Fig. 5 shows the S1 and S2 waveforms of the event labeled as "Event A" in Fig. 4. The narrow, flat-top shape of the S2 pulses reveals that this is an event that originated near the liquid surface, where electron diffusion is limited due to the short drift length. The true S1 pulse can actually be seen on the left of the first S2 pulse. However, it was merged into the S2 by the pulse reconstruction algorithm. Given that the true drift length of the energy deposit that created the S2 pulses is of the order of a few microseconds, the reconstructed S1 pulses happening hundreds of microseconds apart cannot have originated from the same energy deposit.

The total signal acceptance, shown in Fig. 6, was evaluated from the sample of simulated MIMP events. The fiducial, uniformity, and velocity cuts have the largest impact on the total signal acceptance, with a more pronounced effect for increasing cross sections. At cross sections above 10^{-30} cm^2 the acceptance drops significantly, mostly due to the velocity cut. This is due to a noticeable increase in pulse merging, as was shown in Fig. 2, causing the reconstructed velocity to be outside the cut boundaries and increasing the clustering probability of individual scatters in the multiple-scatter event.

IV. RESULTS AND DISCUSSION

The effect of each analysis cut on the SR1 dataset is shown in Table I. The last column shows the number of events surviving each cut, reaching a total count of zero after we apply all data selection cuts. Dark matter models for which the expected number of signal events exceeds 2.44 (after accounting for the signal acceptance shown in Fig. 6) are excluded at 90% confidence level, which follows the Feldman-Cousins convention for an observation of zero events and a mean background of zero events [49]. We show these limits in Fig. 7, labeled "LZ SR1 MS," alongside previous limits derived from similar multiscatter searches conducted by other experiments [28–31].

In addition to the limits obtained from this multiple-scatter analysis, we extend limits based on the LZ SR1 WIMP search presented in Ref. [10] to high masses and cross sections, labeled in Fig. 7 as LZ SR1 SS. In that publication, limits are displayed up to a mass of 10 TeV/c^2; at this mass, a WIMP model on the limit curve would yield 4.4 expected signal events based on the

TABLE I. List of data analysis cuts applied to the SR1 dataset to search for MIMPs. The number of surviving events after each cut is indicated in the last column.

Name	Description	Events
Initial selection	See Sec. III	10137
Multiplicity	> 1 S1s; > 1 S2s	1538
Good S1	No S1s are overly concentrated in one PMT or have a coincident signal in the OD	1400
Fiducial	≥ 2 S2s with z $\in (2, 135)$ cm and $r < 70$ cm	269
Collinearity	Reduced $\chi^2 < 2$; scatters are causally ordered along the track	237
Uniformity	Scatters are distributed along the track uniformly	67
Velocity	Reconstructed $v \in (50, 1200)$ km/s	11
ROI	Total S1 and total S2 area is within signal region	0

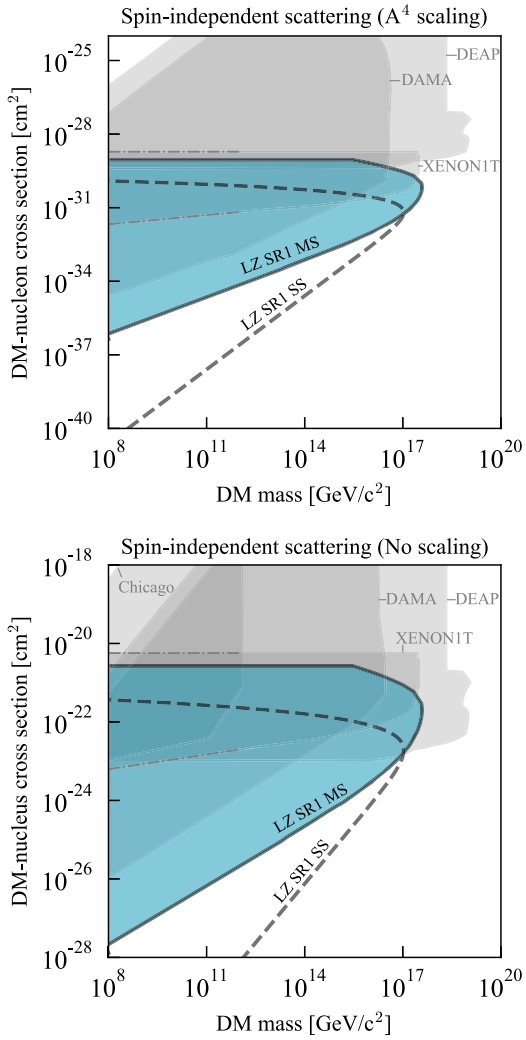

FIG. 7. The 90% confidence level upper limit on the DM scattering cross section as a function of DM mass assuming two contrasting models of scattering with the nucleus. First, a coherent, spin-independent scattering (top); second, a noncoherent scattering between a dark matter particle and the nucleus (bottom). An A^4 scaling arises in the first case due to the coherent and kinematic enhancements of the signal rate (see text). The results from the MIMP search analysis are shown as solid lines, while the extrapolated limits from the WIMP search analysis in Ref. [10] are shown as dashed lines. Constraints from other experiments are also shown: XENON1T [28], DEAP [29], DAMA [30], and Chicago [31]. The extrapolation of the constraint set by XENON1T to lower masses is shown with a dash-dotted gray line.

results from the corresponding PLR analysis. This result is extrapolated to high masses along a contour with an equal expected number of signal events. This extrapolation is justified by the fact that the expected recoil rate spectrum is independent of mass for dark matter masses much greater than the xenon atomic mass [46–48]. Note that this limit cannot be extrapolated indefinitely since only a negligible amount of dark matter transits at high cross sections will produce one scatter (those transits that result in more than one scatter are removed by the single-scatter requirement [10]). This effect sets a ceiling on the SS limit, as shown in Fig. 7. In addition, the fact that the number of single scatters decreases while the number of multiple scatters increases for increasing cross section values explains why the LZ SR1 MS limits have higher reach. The MS analysis has superior signal acceptance at high cross sections and can yield exclusion limits that reach larger masses compared to the SS analysis.

We assume two different dark matter models for the limits shown in Fig. 7. Instead of carrying out a comprehensive study of theoretical models, we focus our attention to showing the results of this search under two contrasting models. First, the upper panel of Fig. 7 shows the exclusion limits assuming the cross section model that is typically adopted in direct detection searches. This assumes a spin-independent DM-nuclear scattering in which the total DM-nucleus cross section ($\sigma_{\chi N}$) is coherently enhanced with respect to the DM-nucleon cross section ($\sigma_{\chi n}$). In this case, the differential cross section for the DM-nucleus elastic scattering takes the form [48,50]

$$\frac{d\sigma_{\chi N}}{dE_R} = \frac{d\sigma_{\chi n}}{dE_R}\left(\frac{\mu_{\chi N}}{\mu_{\chi n}}\right)^2 A^2 |F_N(q)|^2, \tag{3}$$

where E_R is the recoil energy of the nucleus, $\mu_{\chi N}$ and $\mu_{\chi n}$ are the reduced masses of the DM-nucleus and DM-nucleon cross sections, respectively, A is the number of nucleons in the nucleus, and $F_N(q)$ is the nuclear form factor, for which we consider the Helm form factor [51]. In the heavy dark matter limit, a factor of A^2 arises from the ratio of the two reduced masses, resulting in the expression

$$\frac{d\sigma_{\chi N}}{dE_R} = \frac{d\sigma_{\chi n}}{dE_R} A^4 |F_N(q)|^2. \tag{4}$$

Note that the derivation of this relationship assumes a regime of low interaction strength, so the A^4 scaling may not be a reasonable assumption for high DM-nucleon cross sections [52]. Precise scaling between the DM-nucleon and DM-nucleus cross sections is dependent on the choice of the interaction potential. Additionally, at high masses where composite dark matter models are especially relevant, it may be required to consider a form factor term not only for the nucleus but also for the dark matter particle [19]. We leave a more comprehensive study of alternative dark matter models to future publications.

Second, we consider a contact interaction model with no coherent enhancement of the per-nucleon cross section, taking the form

$$\frac{d\sigma_{\chi N}}{dE_R} = \frac{d\sigma_{\chi n}}{dE_R} |F_N(q)|^2. \tag{5}$$

This model has also been selected as an additional benchmark for the sensitivity of high cross section dark matter searches in other studies [28,53,54]. Without the A^4 enhancement, the heavier xenon nucleus loses some advantage in probing dark matter at low cross sections. This is apparent in the lower panel of Fig. 7, which shows an increased overlap between the LZ MS limit and previous constraints using other target elements [29–31].

With the results from this analysis, we are able to probe an intermediate parameter space between the LZ SR1 SS limit and MS limits set by other experiments [28–31]. In the LZ SR1 MS analysis, MIMP signals must include well-separated S1s and S2s. At high cross sections, the LZ SR1 MS analysis loses sensitivity when multiple pulses are no longer resolvable, causing the "turnaround" at high masses. By contrast, similar searches by DEAP-3600 [54] and XENON1T [28] seek a MIMP signal topology consisting of single pulses with anomalous shape caused by the merging of many closely spaced signals. Consequently, the limits from those searches can extend to higher cross section, but their sensitivity to dark matter models resulting in a low multiplicity of scatters (i.e., low cross section) is heavily constrained.

V. CONCLUSIONS

By considering transiting dark matter that has a high probability of interacting within its path length across the LZ TPC detector, such that multiple scatters become likely, we demonstrated that LZ can extend its sensitivity to dark matter models of high masses and high cross sections. The low energy threshold and large surface area of LZ makes this kind of search favorable. After data selection, we did not observe any event that was consistent with a transiting MIMP in the SR1 dataset. Based on this result, we set competitive per-nucleus limits and world-leading per-nucleon limits for dark matter at high mass. The maximum mass probed by LZ is extended to 3.9×10^{17} GeV$/c^2$ compared to an extrapolation of the WIMP search exclusion limit from Ref. [10]. In the full exposure of 1000 day live days and assuming a similar total acceptance as the one shown in Fig. 6, we predict LZ will probe dark matter masses up to 6.5×10^{18} GeV$/c^2$.

Additionally, the rich information in MIMP events, especially full reconstruction of the velocity vector, will be valuable for confirming the dark matter origin as well as reconstructing dark matter properties in the event of the observation of this type of signal. For some models, the single- and multiple-scatter channels can provide complementary information that will be essential to investigate any excess observed in the data.

Selected data from the following plots can be accessed at [55]:

(i) Figure 6: points representing the total acceptance curve for the multiple-scatter analysis (black line).

(ii) Figure 7: points representing the 90% confidence level upper limits assuming two contrasting dark matter models: first, a spin-independent scattering model in which the differential cross section for the DM-nucleus elastic scattering scales as A^4 with the DM-nucleon elastic scattering differential cross section (A is the nuclear mass number); second, a spin-independent scattering model in which no coherent enhancement of the per-nucleon cross section is assumed. Two limits are shown in each case: the upper limit corresponding to the MIMP search analysis (solid line) and the extrapolated limit from the WIMP search analysis to high dark matter masses (dashed line) [10]. The points are expressed in units of GeV$/c^2$ and cm^2 for mass and cross section, respectively.

ACKNOWLEDGMENTS

We thank Rafael Lang, Shengchao Li, Shawn Westerdale, and Joseph Bramante for insightful discussions. The research supporting this work took place in part at Sanford Underground Research Facility (SURF) in Lead, South Dakota. Funding for this work is supported by the U.S. Department of Energy, Office of Science, Office of High Energy Physics under Contracts No. DE-AC02-05CH11231, No. DE-SC0020216, No. DE-SC0012704, No. DE-SC0010010, No. DE-AC02-07CH11359, No. DE-SC0012161, No. DE-SC0015910, No. DE-SC0014223, No. DE-SC0010813, No. DE-SC0009999, No. DE-NA0003180, No. DE-SC0011702, No. DE-SC0010072, No. DE-SC0015708, No. DE-SC0006605, No. DE-SC0008475, No. DE-SC0019193, No. DE-FG02-10ER46709, No. UW PRJ82AJ, No. DE-SC0013542, No. DE-AC02-76SF00515, No. DE-SC0018982, No. DE-SC0019066, No. DE-SC0015535, No. DE-SC0019319, No. DE-AC52-07NA27344, No. DOE-SC0012447, and No. DE-SC0024225. This research was also supported by U.S. National Science Foundation (NSF); the UKRI's Science and Technology Facilities Council under Awards No. ST/M003744/1, No. ST/M003655/1, No. ST/M003639/1, No. ST/M003604/1, No. ST/M003779/1, No. ST/M003469/1, No. ST/M003981/1, No. ST/N000250/1, No. ST/N000269/1, No. ST/N000242/1, No. ST/N000331/1, No. ST/N000447/1, No. ST/N000277/1, No. ST/N000285/1, No. ST/S000801/1, No. ST/S000828/1, No. ST/S000739/1, No. ST/S000879/1, No. ST/S000933/1, No. ST/S000844/1, No. ST/S000747/1, No. ST/S000666/1, No. ST/R003181/1; Portuguese Foundation for Science and Technology (FCT) under Award No. PTDC/FIS-PAR/2831/2020; the Institute for Basic Science, Korea (Budget No. IBS-R016-D1). We acknowledge additional support from the STFC Boulby Underground Laboratory in the UK, the GridPP [56,57] and IRIS Collaborations, in particular at Imperial College

London and additional support by the University College London (UCL) Cosmoparticle Initiative. We acknowledge additional support from the Center for the Fundamental Physics of the Universe, Brown University. K. T. L. acknowledges the support of Brasenose College and Oxford University. The LZ Collaboration acknowledges key contributions of Dr. Sidney Cahn, Yale University, in the production of calibration sources. This research used resources of the National Energy Research Scientific Computing Center, a DOE Office of Science User Facility supported by the Office of Science of the U.S. Department of Energy under Contract No. DE-AC02-05CH11231. We gratefully acknowledge support from GitLab through its GitLab for Education Program. The University of Edinburgh is a charitable body, registered in Scotland, with the Registration No. SC005336. The assistance of SURF and its personnel in providing physical access and general logistical and technical support is acknowledged. We acknowledge the South Dakota Governor's office, the South Dakota Community Foundation, the South Dakota State University Foundation, and the University of South Dakota Foundation for use of xenon. We also acknowledge the University of Alabama for providing xenon.

[1] N. Aghanim *et al.* (Planck Collaboration), Astron. Astrophys. **641**, A6 (2020); **652**, C4(E) (2021).
[2] Y. Sofue and V. Rubin, Annu. Rev. Astron. Astrophys. **39**, 137 (2001).
[3] D. Harvey, R. Massey, T. Kitching, A. Taylor, and E. Tittley, Science **347**, 1462 (2015).
[4] J. Einasto, *Dark Matter and Cosmic Web Story* (World Scientific Publishing Co., Singapore, 2014).
[5] A. Arbey and F. Mahmoudi, Prog. Part. Nucl. Phys. **119**, 103865 (2021).
[6] G. Bertone, D. Hooper, and J. Silk, *Particle Dark Matter: Observations, Models and Searches*, edited by G. Bertone (Cambridge University Press, Cambridge, England, 2010).
[7] G. Bertone and D. Hooper, Rev. Mod. Phys. **90**, 045002 (2018).
[8] M. Schumann, J. Phys. G **46**, 103003 (2019).
[9] A. S. Chou *et al.*, arXiv:2211.09978.
[10] J. Aalbers *et al.* (LZ Collaboration), Phys. Rev. Lett. **131**, 041002 (2023).
[11] D. S. Akerib *et al.* (LZ Collaboration), Nucl. Instrum. Methods Phys. Res., Sect. A **953**, 163047 (2020).
[12] D. Carney *et al.*, SciPost Phys. Core **6**, 075 (2023).
[13] E. W. Kolb and A. J. Long, Phys. Rev. D **96**, 103540 (2017).
[14] N. Okada and O. Seto, Phys. Lett. B **820**, 136528 (2021).
[15] D. M. Grabowska, T. Melia, and S. Rajendran, Phys. Rev. D **98**, 115020 (2018).
[16] A. Coskuner, D. M. Grabowska, S. Knapen, and K. M. Zurek, Phys. Rev. D **100**, 035025 (2019).
[17] G. Krnjaic and K. Sigurdson, Phys. Lett. B **751**, 464 (2015).
[18] E. Hardy, R. Lasenby, J. March-Russell, and S. M. West, J. High Energy Phys. 06 (2015) 011.
[19] E. Hardy, R. Lasenby, J. March-Russell, and S. M. West, J. High Energy Phys. 07 (2015) 133.
[20] M. I. Gresham, H. K. Lou, and K. M. Zurek, Phys. Rev. D **96**, 096012 (2017).
[21] A. Bhoonah, J. Bramante, S. Schon, and N. Song, Phys. Rev. D **103**, 123026 (2021).
[22] J. S. Wu, V. Brien, P. Brunet, C. Dong, and J. M. Dubois, Philos. Mag. Part A **80**, 1645 (2000).
[23] A. Bhoonah, J. Bramante, B. Courtman, and N. Song, Phys. Rev. D **103**, 103001 (2021).
[24] P. W. Graham, R. Janish, V. Narayan, S. Rajendran, and P. Riggins, Phys. Rev. D **98**, 115027 (2018).
[25] J. F. Acevedo, J. Bramante, and A. Goodman, J. Cosmol. Astropart. Phys. 11 (2023) 085.
[26] J. Bramante, B. Broerman, R. F. Lang, and N. Raj, Phys. Rev. D **98**, 083516 (2018).
[27] A. Bhoonah, J. Bramante, F. Elahi, and S. Schon, Phys. Rev. D **100**, 023001 (2019).
[28] E. Aprile *et al.* (XENON Collaboration), Phys. Rev. Lett. **130**, 261002 (2023).
[29] P. Adhikari *et al.* (DEAP Collaboration), Phys. Rev. Lett. **128**, 011801 (2022).
[30] R. Bernabei *et al.*, Phys. Rev. Lett. **83**, 4918 (1999).
[31] C. V. Cappiello, J. I. Collar, and J. F. Beacom, Phys. Rev. D **103**, 023019 (2021).
[32] I. F. M. Albuquerque and C. Perez de los Heros, Phys. Rev. D **81**, 063510 (2010).
[33] I. F. M. Albuquerque and L. Baudis, Phys. Rev. Lett. **90**, 221301 (2003); **91**, 229903(E) (2003).
[34] B. J. Kavanagh, Phys. Rev. D **97**, 123013 (2018).
[35] D. S. Akerib *et al.* (LUX Collaboration), Phys. Rev. D **97**, 102008 (2018).
[36] D. Akerib *et al.*, J. Instrum. **13**, P02001 (2018).
[37] Table de Radionucléides, Bi-212, http://www.lnhb.fr/nuclides/Bi-212_tables.pdf.
[38] Table de Radionucléides, Bi-214, http://www.lnhb.fr/nuclides/Bi-214_tables.pdf.
[39] D. S. Akerib *et al.* (LZ Collaboration), Phys. Rev. C **102**, 014602 (2020).
[40] J. Aalbers *et al.* (LZ Collaboration), Phys. Rev. D **108**, 012010 (2023).
[41] D. Baxter *et al.*, Eur. Phys. J. C **81**, 907 (2021).
[42] D. S. Akerib *et al.* (LZ Collaboration), Astropart. Phys. **125**, 102480 (2021).

[43] J. Allison *et al.*, Nucl. Instrum. Methods Phys. Res., Sect. A **835**, 186 (2016).
[44] J. R. Watson, High voltage considerations for dark matter searches, Ph.D. thesis, University of California, 2022.
[45] D. S. Akerib *et al.* (LUX Collaboration), Phys. Rev. D **102**, 092004 (2020).
[46] J. Lewin and P. Smith, Astropart. Phys. **6**, 87 (1996).
[47] D. G. Cerdeño and A. M. Green, Direct detection of WIMPS, in *Particle Dark Matter: Observations, Models and Searches*, edited by G. Bertone (Cambridge University Press, Cambridge, England, 2010), pp. 347–369.
[48] A. H. Peter, V. Gluscevic, A. M. Green, B. J. Kavanagh, and S. K. Lee, Phys. Dark Universe **5–6**, 45 (2014), Hunt for Dark Matter.
[49] G. J. Feldman and R. D. Cousins, Phys. Rev. D **57**, 3873 (1998).
[50] E. Armengaud, C. R. Phys. **13**, 730 (2012), Understanding the Dark Universe.
[51] L. Vietze, P. Klos, J. Menéndez, W. C. Haxton, and A. Schwenk, Phys. Rev. D **91**, 043520 (2015).
[52] M. C. Digman, C. V. Cappiello, J. F. Beacom, C. M. Hirata, and A. H. G. Peter, Phys. Rev. D **100**, 063013 (2019); **106**, 089902(E) (2022).
[53] M. Clark, A. Depoian, B. Elshimy, A. Kopec, R. F. Lang, S. Li, and J. Qin, Phys. Rev. D **102**, 123026 (2020).
[54] R. Ajaj *et al.* (DEAP Collaboration), Phys. Rev. D **100**, 022004 (2019).
[55] I. Olcina and R. Smith, HEPData v1 (2024), https://www.hepdata.net/record/ins2758452?version=1.
[56] P. Faulkner *et al.*, J. Phys. G **32**, N1 (2005).
[57] D. Britton *et al.*, Phil. Trans. R. Soc. A **367**, 2447 (2009).